

Critical Analysis of Thermodiffusion-Induced Unipolar Resistive Switching in a Metal-Oxide-Metal Memristive Device

Kristof Lange,* Rainer Waser, and Stephan Menzel*

It has been previously proposed that the SET and RESET processes in a unipolar switching metal-oxide-metal memristive device can be explained by thermodiffusion only. In order to validate this, time-dependent finite element method simulations are performed in a purely theoretical study. To that end, a range of configurations regarding device geometry and various parameters is used. In particular, this includes simulations using different activation enthalpies for oxygen vacancy transport, different radii for the top electrode, and different time constants for the applied voltage or current. When the top electrode is smaller than the other layers by a sufficient margin, a temperature gradient emerges that in turn leads to a transport of oxygen vacancies toward the center of the oxide. This effect can be interpreted as a SET. In a system with low activation enthalpy for vacancy transport, i.e., 0.4 eV or less, the effect is volatile, while it is nonvolatile for activation enthalpies of 0.9 eV or more. However, in the latter case, a RESET is not possible. Therefore, further effects other than thermodiffusion must be taken into account in the description of unipolar resistive switching.

1. Introduction

By applying an external electrical signal, a memristive device can be switched between two or more distinct states of electrical resistance. A transition into a state with lower resistance is called a SET, while the opposite is called RESET. Bipolar memristive devices use different signal polarities for their SET and RESET. Unipolar devices typically have lower endurance when compared to their bipolar counterparts.^[1,2] However, they require only a single polarity of the applied signal for operation, making them attractive for resistive switching arrays as this allows for simplified circuit design.^[3]

In a unipolar device, SET and RESET are controlled by the absolute values of the applied voltage and current, irrespective of their polarity. During the SET process, the current is limited by a current compliance, whereas this limit is removed during

the RESET process. Consequently, the absolute value of the current is highest for the RESET, while the absolute SET voltage is higher than the absolute RESET voltage.^[4]


The asymmetric behavior of a bipolar metal-oxide-metal memristive device stems from the use of dissimilar materials for the metal electrodes. One electrode, called the active electrode, shows a Schottky characteristic at the interface, while the other one forms an ohmic contact and is therefore called the ohmic electrode.^[1] In such a device, the switching process is commonly ascribed to a change in oxygen vacancy concentration at the active electrode, i.e., a vacancy transport along the direction of the electrical current.

On the other hand, a unipolar device is symmetrical in terms of its electrical characteristics, which lends itself to a description in terms of thermal effects. One such effect is the transport of oxygen vacancies along a temperature gradient, also called thermodiffusion or Soret diffusion, which occurs mainly in the radial direction perpendicular to the electrical current. The idea is that during SET, the oxygen vacancies are pulled along a high temperature gradient toward the hottest point at the center of the oxide. Under the assumption of a low temperature gradient during RESET, oxygen vacancies would diffuse back outward along concentration gradients. Strukov et al. proposed that this by itself could explain the switching of unipolar devices; however, their description is limited by the assumption of static temperature profiles during switching.^[5]

K. Lange, R. Waser
Institut für Werkstoffe der Elektrotechnik II (IWE2)
RWTH Aachen University
52074 Aachen, Germany
E-mail: k.lange@iwe.rwth-aachen.de

R. Waser, S. Menzel
Peter Grünberg Institut 7 (PGI-7)
Forschungszentrum Jülich GmbH
52425 Jülich, Germany
E-mail: st.menzel@fz-juelich.de

R. Waser
Peter Grünberg Institut 10 (PGI-10)
Forschungszentrum Jülich GmbH
52425 Jülich, Germany

 The ORCID identification number(s) for the author(s) of this article can be found under <https://doi.org/10.1002/pssa.202300407>.

© 2023 The Authors. physica status solidi (a) applications and materials science published by Wiley-VCH GmbH. This is an open access article under the terms of the Creative Commons Attribution-NonCommercial License, which permits use, distribution and reproduction in any medium, provided the original work is properly cited and is not used for commercial purposes.

DOI: 10.1002/pssa.202300407

As a dynamic model in support of this idea is not available yet, we performed time-dependent finite element method (FEM) simulations to validate if thermodiffusion by itself is sufficient to explain the SET and RESET processes in unipolar metal-oxide-metal memristive devices.

2. Simulation Setup

All our simulations were performed using the commercial finite element software package COMSOL Multiphysics. In general, the device used for all simulations consists of a top electrode, an oxide layer, a bottom electrode, and a substrate. **Figure 1** gives a schematic overview of the axially symmetric 2D structure. The bottom of the substrate acts as a heat sink at a constant temperature of 293.15 K, with all other exterior surfaces thermally insulated. An electrical ground plane exists at the interface between the substrate and the bottom electrode, and the electrical voltage or current signal is applied to the top electrode. The radius of the top electrode is half that of the other layers.

The equation system for the simulation contains three equations for the three state variables electric potential V , temperature T , and oxygen vacancy concentration c . Given the applied voltage or current, the electric potential is calculated by the static current continuity equation

$$\nabla \cdot \mathbf{J} = -\nabla \cdot (\sigma \nabla V) = 0 \quad (1)$$

where \mathbf{J} is the electric current and σ is the electrical conductivity. Temperature profiles are calculated with the time-dependent heat transfer equation

$$\rho C_p \frac{\partial T}{\partial t} = \nabla \cdot (\kappa \nabla T) - \mathbf{J} \cdot \nabla V \quad (2)$$

using the density ρ , the heat capacity C_p , and the thermal conductivity κ .

Starting with the Fick diffusion along concentration gradients and the Soret diffusion along temperature gradients, the continuity equation for oxygen vacancies becomes

$$\frac{\partial c}{\partial t} = \nabla \cdot (D \nabla c + D_T c \nabla T) \quad (3)$$

Here, D and D_T denote the diffusion coefficients for Fick diffusion

$$D = D_0 \exp\left(-\frac{\Delta H}{k_B T}\right) \left(1 - \frac{c}{c_{\max}}\right) \quad (4)$$

and Soret diffusion

$$D_T = S_T D = -\frac{\Delta H}{k_B T^2} D \quad (5)$$

where ΔH is the activation enthalpy for vacancy transport, k_B is the Boltzmann constant, and S_T is the Soret factor. The diffusion prefactor is given by $D_0 = 10^{-6} \frac{\text{m}^2}{\text{s}}$. The values for the maximum concentration and the activation enthalpy are given by $c_{\max} = 10^{28} \text{ m}^{-3}$ and $\Delta H = 1 \text{ eV}$, respectively.

The simulation does not account for drift along the gradient of the electric potential as we assume electrically neutral vacancies in order to focus on thermal effects. Otherwise, drift forces would be significantly greater than diffusion forces.

In **Table 1**, the material parameters used for the simulation are listed.^[6] The electrical conductivity of the oxide is given by

$$\sigma_{\text{TaO}_x} = \sigma_0 \frac{c}{c_{\max}}, \quad \sigma_0 = 7.5 \times 10^4 \frac{\text{S}}{\text{m}} \quad (6)$$

and therefore depends linearly on the oxygen vacancy concentration.

Initially, the vacancies are distributed uniformly throughout the oxide at a concentration of $c_0 = 10^{25} \text{ m}^{-3}$. The total number of vacancies in the oxide stays constant during the simulation, which is why the concentration is only calculated in the oxide. On the other hand, the temperature is calculated in all layers, while the substrate is excluded for the calculation of the electric potential.

3. Simulation Results

3.1. Evolution of Temperature and Concentration Profiles

Horizontal and vertical profiles of the oxygen vacancy concentration and temperature at different times are shown in **Figure 2**, with the location of the cut lines with respect to the 2D structure sketched in **Figure 3a**. The applied signal is a linear voltage ramp

Table 1. List of material parameters.

	TiN	TaO _x	SiO ₂
$\sigma \left[\frac{\text{S}}{\text{m}} \right]$	5×10^6	user defined	–
ϵ_r	4	22	–
$\kappa \left[\frac{\text{W}}{\text{m} \cdot \text{K}} \right]$	5	4	1.4
$C_p \left[\frac{\text{J}}{\text{kg} \cdot \text{K}} \right]$	545	174	730
$\rho \left[\frac{\text{kg}}{\text{m}^3} \right]$	5210	8200	2200

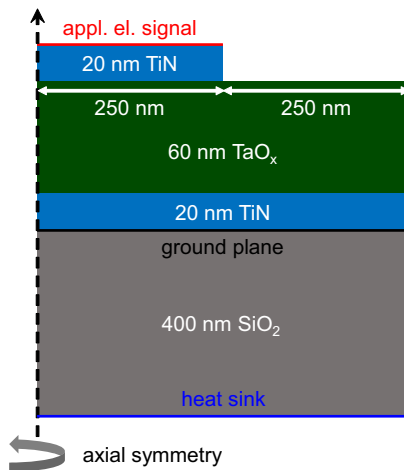


Figure 1. 2D structure with axial symmetry in a schematic overview that includes the boundary conditions for temperature and electrical potential or current.

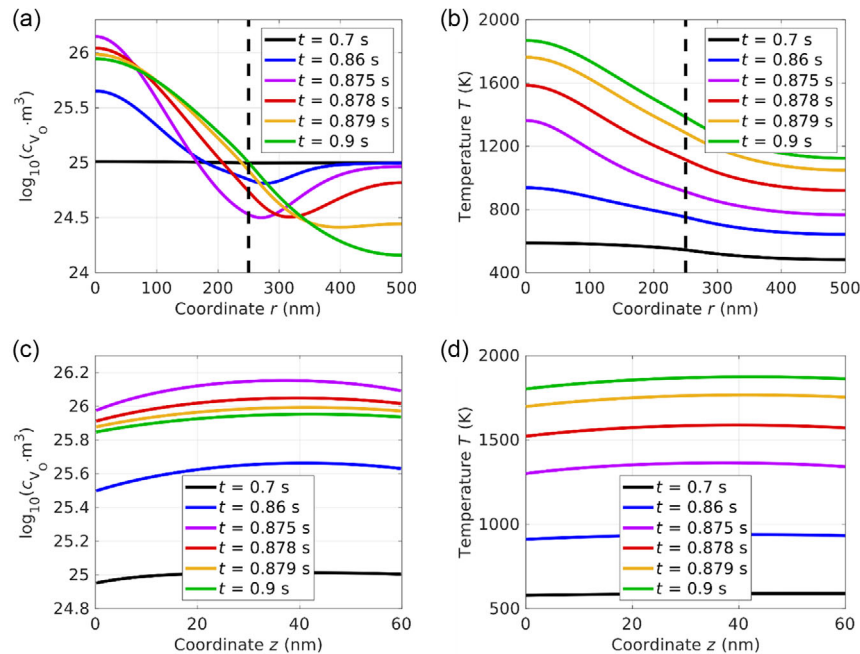


Figure 2. Profiles of oxygen vacancy concentration and temperature along the horizontal and vertical cut lines shown in Figure 3 at selected times t , showing the evolution over time. The vertical dashed lines in subfigures (a,b) mark the top electrode radius. a) Vacancy concentration along a horizontal cut line. b) Temperature along the same horizontal cut line. c) Vacancy concentration along a vertical cut line at $r = 0$. d) Temperature along the same vertical cut line.

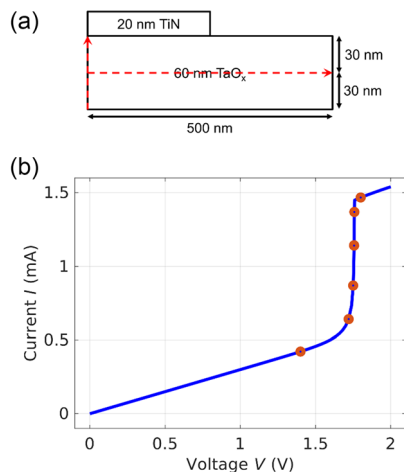


Figure 3. a) Sketch of the location of horizontal and vertical cut lines within the oxide as used in Figure 2, indicated by red dashed arrows. b) Simulated I - V curve for a linear voltage-controlled sweep with a ramping time of 1 s up to a maximum voltage of 2 V. The red circles correspond to the times used in Figure 2.

from 0 to 2 V at a ramping time of 1 s. In Figure 3b, the resulting total current is plotted against the applied voltage, and the times of the cut lines in Figure 2 are marked.

At a voltage of ≈ 1.75 V, there is a sharp increase in current. This coincides with a movement of vacancies toward the center of the oxide, which causes an increase in oxide conductivity. At the same time, the smaller top electrode leads to a radial

temperature gradient that is the driving force behind the oxygen vacancy transport. In contrast, in the axial direction along the flow of electric current, only small temperature gradients evolve within the oxide. Therefore, the vacancy concentration stays much more uniform in that direction.

3.2. Unipolar Nature of SET by Thermodiffusion

The aforementioned transport of oxygen vacancies toward the center of the oxide can be interpreted as an SET event. To demonstrate the nonvolatile nature of this SET event for the given configuration, the applied voltage signal was extended as indicated in Figure 4, where the resulting current and maximum vacancy concentration are also shown. During the first triangular voltage pulse, the maximum oxygen vacancy concentration increases and stays elevated throughout the sweep, even after a second triangular voltage pulse with negative polarity. Not only does this verify that the SET is nonvolatile but it also shows that a RESET is not possible, as the application of a voltage or current signal directly leads to the temperature gradient that causes the vacancy transport in the first place. To check whether this behavior depends on the voltage polarity, a voltage signal with reverse polarity was used, leading to identical results for absolute current and maximum vacancy concentration. A comparison with measurements from other research groups of a bipolar switching TiN/TaO_x/TiN stack and a unipolar switching Pt/TaO_x/Pt stack shows that our SET voltages and currents consistently fall within a reasonable range in terms of their order of magnitude.^[7,8]

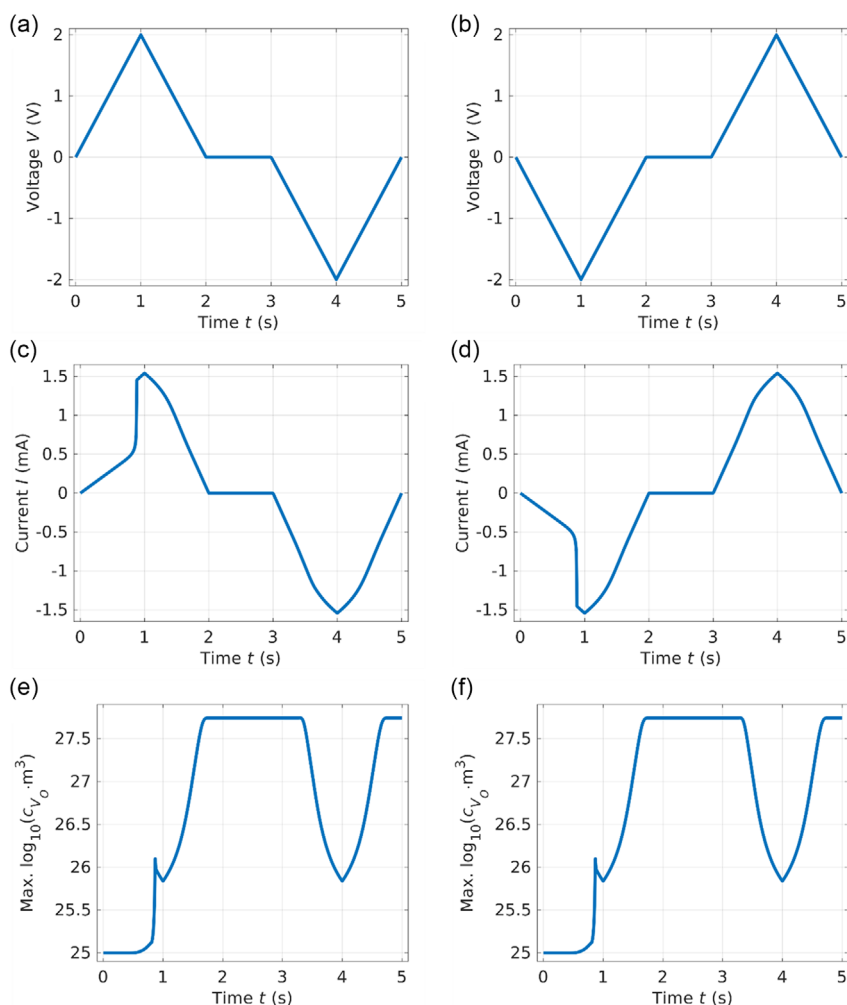


Figure 4. a) Voltage sweep signal, starting with a positive voltage. b) Voltage sweep signal, starting with a negative voltage. c) Current resulting from the applied voltage in subfigure (a). d) Current resulting from the applied voltage in subfigure (b). e) Maximum oxygen vacancy concentration corresponding to subfigure (a). f) Maximum oxygen vacancy concentration corresponding to subfigure (b).

As the Soret factor is proportional to T^{-2} , at high temperatures, the equilibrium between Soret and Fick diffusion is shifted in favor of the latter. This explains the dip in oxygen vacancy concentration during the second voltage pulse, and also the high concentration increase as the voltage returns to 0 V during the first pulse. However, the point that the concentration stays elevated still stands.

3.3. Top Electrode Radius

Figure 5 shows the I - V curves and the maximum oxygen vacancy concentrations and temperatures for different radii of the top electrode r_{top} , given as a factor of the oxide radius r_{ox} . The activation enthalpy remains unchanged at $\Delta H = 1$ eV, and the same value is also used in Sections 3.4 to 3.9. In this case, the same voltage ramp as in Section 3.1 was used, immediately followed by a linear ramp back to 0 V at the same ramping time of 1 s.

For $r_{\text{top}} = r_{\text{ox}}$, no radial vacancy transport occurs since there is no radial temperature gradient. A small increase in the maximum

vacancy concentration is caused by axial transport of oxygen vacancies. In all other cases where $r_{\text{top}} < r_{\text{ox}}$, the radial transport outweighs the axial transport by a few orders of magnitude.

The initial electrical conductance of the device decreases with smaller top electrodes. Therefore, smaller top electrode radii lead to higher SET voltages. Due to the lacking radial vacancy transport, there is no SET event for $r_{\text{top}} = r_{\text{ox}}$, and the I - V curve is linear.

Similar to the discussion in the previous section, after its increase during the SET with $r_{\text{top}} < r_{\text{ox}}$, the maximum vacancy concentration decreases with further increasing voltage and thus temperature. This effect is particularly noteworthy for top electrode radii close to the oxide radius, shown here for a top electrode radius of 450 nm, as there is a dip in temperature directly after the SET. Conversely, as the applied voltage decreases, the temperature increases for a brief time. In this case, the concentration of oxygen vacancies almost returns to its initial value at the peak voltage of the applied signal.

Interestingly, the final maximum vacancy concentrations are similar for all shown cases where the top electrode radius

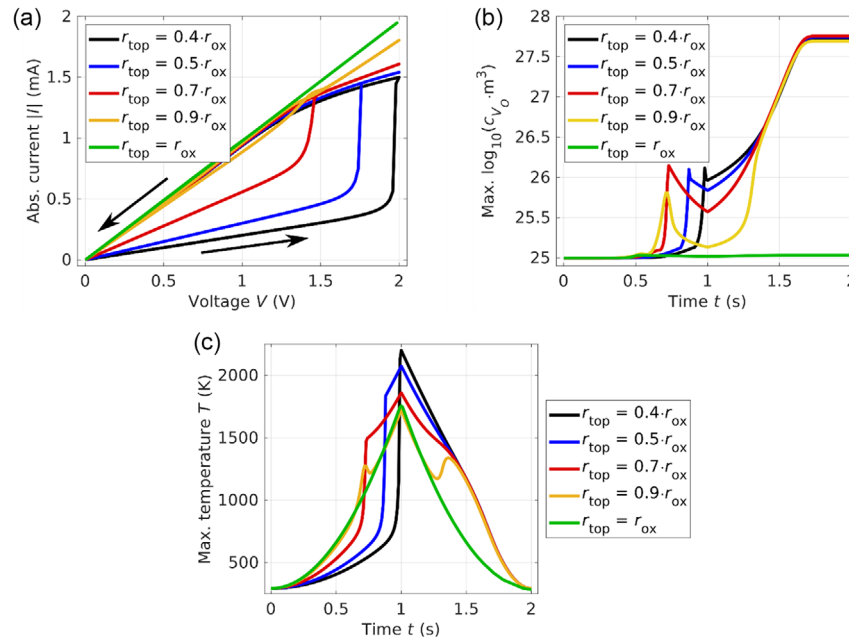


Figure 5. Influence of the top electrode radius for a range of radii. a) I - V curves with arrows indicating the direction of the path. b) Maximum oxygen vacancy concentration. c) Maximum temperature.

differs from the rest of the device. This could be caused by a self-accelerating effect, where a temperature gradient causes an inward radial transport of the oxygen vacancies, which increases the electrical conductivity near the center of the device, causing the temperature gradient to rise further. Due to Soret diffusion being limited at high temperatures, the highest concentration is only reached near the end of the triangular voltage pulse. Especially for $r_{\text{top}} = 0.9 \times r_{\text{ox}}$, during this final increase in the concentration maximum, the vacancy distribution considerably narrows toward the center of the device, as shown in **Figure 6**.

Figure 7 gives a closer view of the final maximum oxygen vacancy concentration, i.e., at time $t = 2$ s, as a function of the top electrode radius. The concentration stays roughly constant up to a radius of $r_{\text{top}} = 450 \text{ nm} = 0.9 \times r_{\text{ox}}$ and then drops

off, underlining the requirement for a sufficiently big difference in radii to get radial vacancy transport.

3.4. Oxide Thickness

As most of the applied voltage is dropped over the oxide, its thickness h_{ox} has a strong correlation to the total device conductance. To study the effect on the SET process, a linearly increasing current was applied to devices where we changed h_{ox} from its default value of 60 nm. While the maximum currents are different, a constant slope of $\partial I / \partial t = 1 \text{ mA s}^{-1}$ was used for all oxide thicknesses. The results are summarized in **Figure 8**. When applying a current-controlled signal, the SET event manifests itself as a region with negative differential resistance in the I - V curves. For thinner oxides, the current required for switching increases, but at the same time, the SET occurs at lower voltages. Because of

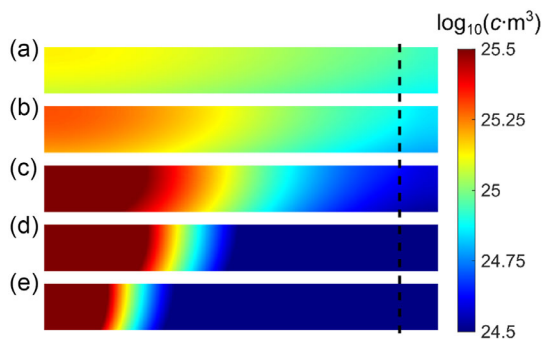


Figure 6. Evolution of the concentration of oxygen vacancies for the falling edge of the voltage sweep as 2D heat maps spanning the entirety of the oxide. The top electrode radius of $r_{\text{top}} = 0.9 \times r_{\text{ox}}$ is marked by a vertical dashed line, revealing that the vacancy distribution gets considerably narrower. a) $t = 1$ s. b) $t = 1.2$ s. c) $t = 1.3$ s. d) $t = 1.4$ s. e) $t = 2$ s.

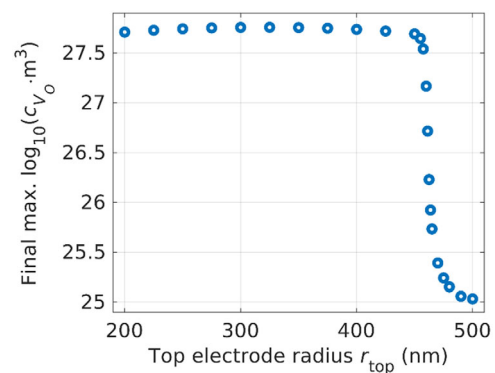


Figure 7. Maximum concentration of oxygen vacancies at $t = 2$ s as a function of r_{top} .

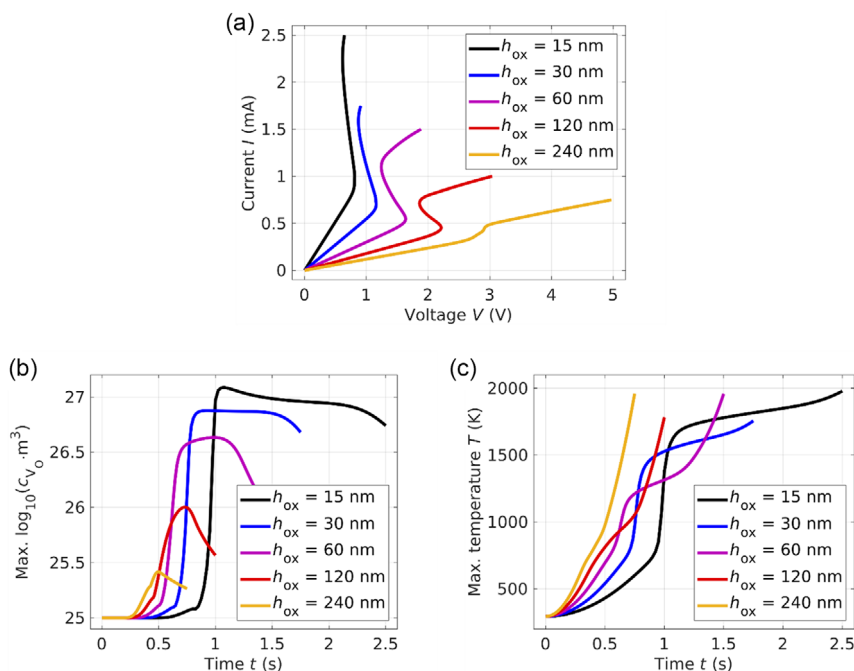


Figure 8. Influence of the oxide thickness on the SET process. a) I - V curves. b) Maximum oxygen vacancy concentration. c) Maximum temperature.

the negative differential resistance, the rate $\partial T / \partial t$ first increases and then decreases during SET. However, the maximum currents were chosen such that temperatures never exceed 2000 K.

In all cases, a complete SET event is observed since the oxygen vacancy concentration is reduced with a further current increase. Notably, with thinner oxides, higher vacancy concentrations are achieved. This is due to higher SET temperatures, which lead to greater temperature gradients.

Figure 9 highlights a further effect observed for thicker oxides. Instead of a mainly radial distribution of oxygen vacancies, a noticeable concentration gradient in the axial direction emerges. This follows the axial temperature gradient, which is more pronounced with higher oxide thicknesses.

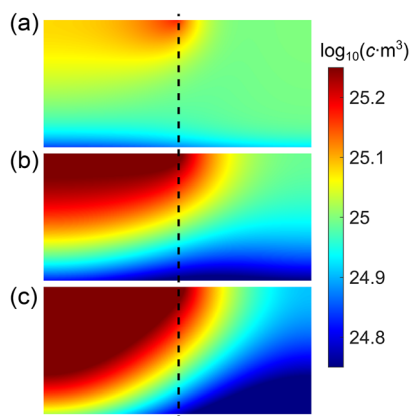


Figure 9. 2D heat maps showing the evolution of the oxygen vacancy distribution for an oxide thickness of $h_{\text{ox}} = 240$ nm. Each snapshot covers the entire oxide. A vertical dashed line marks the top electrode radius at half the oxide radius. a) $t = 0.36$ s. b) $t = 0.42$ s. c) $t = 0.48$ s.

3.5. Electrical Conductivity of Metal Electrodes

To check to what extent the switching behavior is affected by the electrical conductivity of the metal electrodes, denoted in this section simply by σ , we deliberately chose values multiple orders of magnitude below the default value of $\sigma = 5 \times 10^6 \text{ S m}^{-1}$. For all conductivities, the same voltage signal as in Section 3.1 is used: A linear ramp up to 2 V is immediately followed by another linear ramp back to 0 V, after which no signal is applied for 1 s. The sweep is completed by two further linear ramps to -2 V and immediately back to 0 V. Each ramp takes 1 s.

With the peak voltage fixed at 2 V, **Figure 10** shows that the SET during the first voltage ramp is incomplete if the electrical conductivity of the metal electrodes is too low. In these cases, the actual SET voltage is greater than the peak sweep voltage, and the concentration of oxygen vacancies is further increased toward the end of the sweep. Due to the lowered electrical conductance of the whole device, less current is flowing and the reduced peak temperatures are not sufficient for a complete SET. On the other hand, electrodes that are more conductive allow for increased temperatures and thus higher concentrations of oxygen vacancies.

Plotting the voltage at $t = 1$ s along a cut line, which extends from the ground plane to the upper electrical contact and is situated at $r = 0$, as done in Figure 10d, reveals the voltage dropped across the electrodes. As the electrodes become less conductive, the voltage dropped across them increases. At the lowest simulated electrode conductivity of $\sigma = 10^2 \text{ S m}^{-1}$, however, this voltage is reduced again. Conversely, a higher voltage is dropped across the oxide, which in combination with the low electrode conductivity indicates a low oxide electrical conductivity. This is the result of the SET process not being able to advance as far due to lacking temperatures. In contrast to this, for

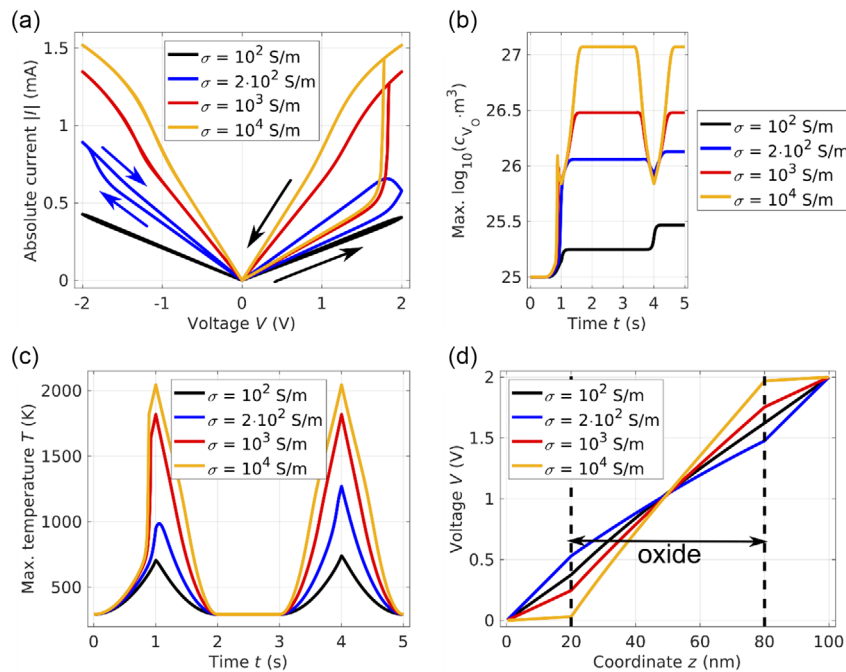


Figure 10. Voltage-controlled sweeps for different electrical conductivities of the metal electrodes. a) I - V curves with the path direction indicated by arrows. b) Maximum oxygen vacancy concentration. c) Maximum temperature. d) Voltages at $t = 1$ s along a cut line at $r = 0$ spanning the oxide and both electrodes. Vertical dashed lines mark the interfaces between the electrodes and the oxide.

$\sigma = 10^4 \text{ S m}^{-1}$, the SET transition is successfully completed, yet almost the entire applied voltage is dropped across the oxide, which is why this case has the lowest external SET voltage.

In summary, an influence of the electrical conductivity of the metal electrodes on the switching behavior is only observed at values at least two orders of magnitude below typical metal conductivities in the order of $\sigma \approx 10^6 \dots 10^7 \text{ S m}^{-1}$.^[9,10]

3.6. Substrate Thermal Conductivity

The SET characteristics of the simulated device are strongly temperature dependent. Aside from the amount of Joule heating, another important aspect is the heat dissipation on which the thermal conductivity of the substrate κ_{sub} has a big influence. For this reason, we ramped the applied voltage up to 2 V and then back to 0 V at a constant rate of 2 V s^{-1} and repeated this for different substrate thermal conductivities. **Figure 11** gives an overview of the results. Before the SET event, the temperature increases more quickly if the substrate is less thermally conductive, causing the SET voltage to be lower.

Although the temperature at which the SET starts is similar in all cases, a more thermally conductive substrate leads to higher temperature gradients within the oxide and therefore an increased transport of oxygen vacancies. This is also reflected in the maximum concentration of oxygen vacancies at the end of the sweep. After the SET event, two counteracting effects determine the temperature. A low thermal conductivity of the substrate means that less Joule heating is required to achieve a certain temperature, but in a device with thermally well conducting substrate, there is more Joule heating due to a higher

electrical conductance after the SET. Overall, the peak temperature at $t = 1$ s increases slightly as κ_{sub} decreases.

3.7. Oxide Thermal Conductivity

At constant levels of Joule heating, a less thermally conductive substrate directly leads to higher oxide temperatures due to better heat retention. In contrast to this, the thermal conductivity of the oxide by itself does not directly affect the average oxide temperature, although it does have an influence on the temperature distribution within the oxide layer. An oxide with low thermal conductivity causes higher internal temperature gradients, resulting in increased Soret diffusion of oxygen vacancies.

As more vacancies accumulate at the center of the device, its conductance rises. Taking into account the increased amount of Joule heating, this leads to higher temperatures immediately after the SET when the oxide is thermally well insulating. This is demonstrated in **Figure 12**, where a linearly increasing current up to 1.2 mA with a ramping time of 1 s was applied. In a thermally well-conducting oxide, more heat needs to be generated to create a sufficient temperature gradient to initiate the SET process, which correlates with a higher SET voltage. At high currents beyond 1.2 mA, this translates to a positive correlation between voltage and oxide thermal conductivity. The higher voltage is the reason for the case with $\kappa_{\text{ox}} = 10 \text{ W (m} \cdot \text{K)}^{-1}$ showing the quickest temperature increase toward the end of the sweep.

In almost all I - V curves, the SET leads to a single continuous region with negative differential resistance. However, for the lowest κ_{ox} , the onset of a negative differential resistance is

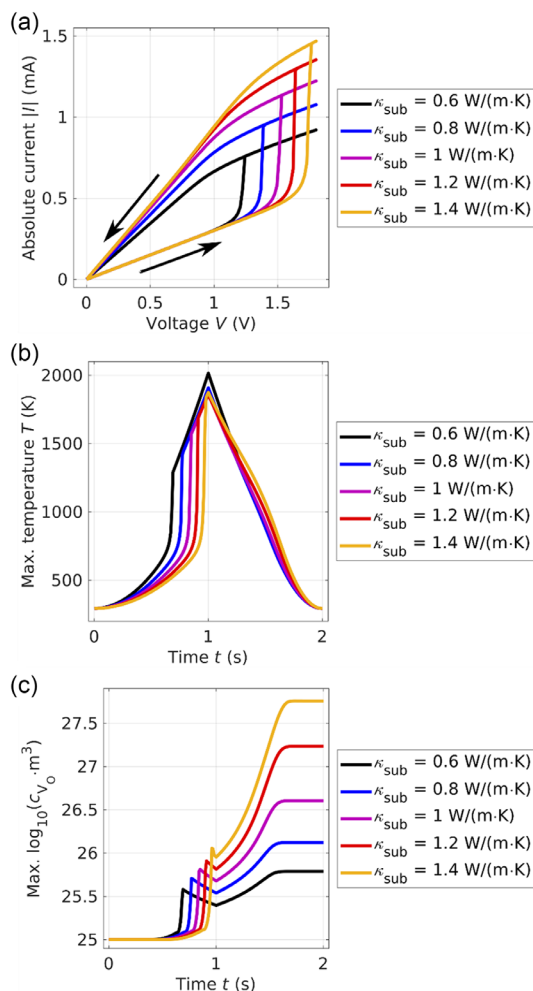


Figure 11. a) I - V curves for a range of substrate thermal conductivities. Arrows indicate the path direction. b) Maximum temperature. c) Maximum oxygen vacancy concentration.

interrupted by a brief increase in voltage. This voltage increase coincides with a redistribution of oxygen vacancies that leads to a smaller radius of the conductive filament, which counters the increase in filament conductivity. While the total device conductance still increases, the rate at which it does so is slowed down enough to interrupt the emergence of negative differential resistance. The smaller filament radius is a consequence of the reduced ability of temperatures to equilibrate if a low thermal conductivity inhibits the heat transfer within the oxide. **Figure 13** is a visualization of the stronger heat confinement at low κ_{ox} and the resulting smaller conductive filaments.

3.8. Diffusion Prefactor

In our model, the mobility of oxygen vacancies can be directly tuned via their diffusion prefactor D_0 . It follows that with lower D_0 , the temperature necessary to start the SET process increases, and thus the SET voltage is also higher. This is visualized in **Figure 14** for a set of diffusion prefactors. As in Section 3.6,

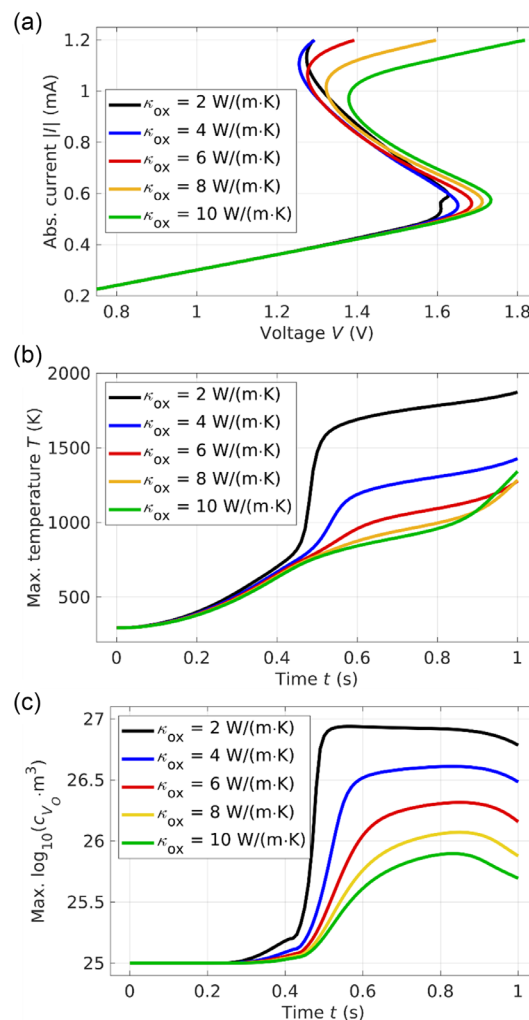


Figure 12. Effect on the SET characteristics of varying the oxide thermal conductivity. a) I - V curves. b) Maximum temperature. c) Maximum oxygen vacancy concentration.

we applied two linear voltage ramps, up to 2 V and back to 0 V, with each ramp taking 1 s. At $t = 1$ s, the device state shows no dependence on D_0 in terms of peak temperature and maximum oxygen vacancy concentration. Despite this, at the end of the sweep, the maximum concentrations differ due the ability of a device with higher diffusion prefactor to react more easily to the shifting equilibrium between Soret and Fick diffusion. This effect is countered in part by a higher mobility at lower temperatures, where the equilibrium shifts back in favor of Fick diffusion as the temperature gradients get smaller.

3.9. Ramping Time

To study the dynamics of the SET by thermodiffusion, in our simulation, we applied a linearly increasing current up to 1.5 mA and varied the time taken for ramping up the current, t_{rise} , over multiple orders of magnitude. A top electrode radius half as big as the oxide radius, serving as the default value, was used for this study, as well as the studies in Sections 3.4 to 3.8

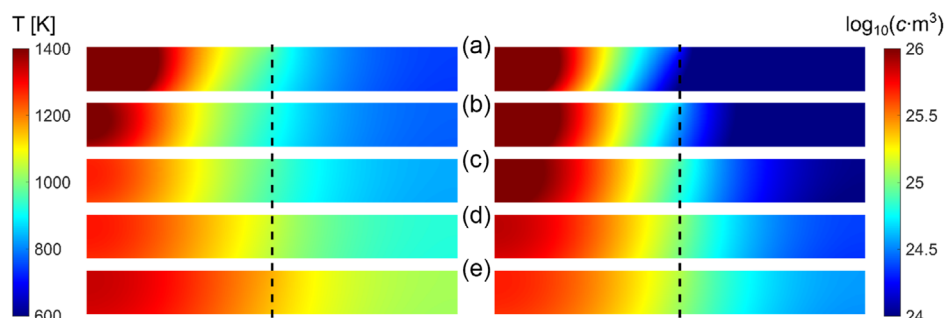


Figure 13. Snapshots of the temperature (left) and maximum oxygen vacancy concentration (right) at time $t = 1 \text{ s}$ for different thermal conductivities of the oxide. Each snapshot shows the entire oxide layer, with vertical dashed lines indicating the top electrode radius. a) $\kappa_{\text{ox}} = 2 \text{ W (m} \cdot \text{K)}^{-1}$. b) $\kappa_{\text{ox}} = 4 \text{ W (m} \cdot \text{K)}^{-1}$. c) $\kappa_{\text{ox}} = 6 \text{ W (m} \cdot \text{K)}^{-1}$. d) $\kappa_{\text{ox}} = 8 \text{ W (m} \cdot \text{K)}^{-1}$. e) $\kappa_{\text{ox}} = 10 \text{ W (m} \cdot \text{K)}^{-1}$.

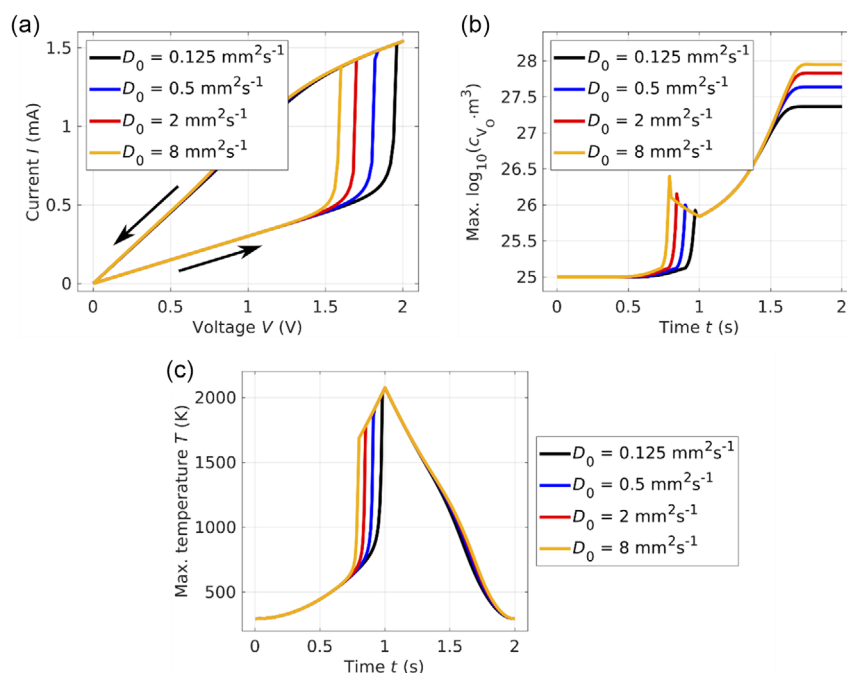


Figure 14. a) I - V curves for a range of oxygen vacancy diffusion prefactors. Arrows indicate the path direction. b) Maximum temperature. c) Maximum oxygen vacancy concentration.

and in Section 3.10. As shown in **Figure 15**, a change of t_{rise} has a strong impact on not only the SET voltage and current but also the oxygen vacancy concentration reached during the SET.

The voltages and currents at which the system starts to show a negative differential resistance decrease for longer t_{rise} . As these points mark the SET event, a slower current ramp allows for lower SET voltage and current, since the system is given more time to approach an equilibrium between Soret and Fick diffusion. At the SET event, the temperature quickly increases, followed by a period of less rapid temperature increase due to the decreasing voltage. Slower current ramps also result in higher peak vacancy concentrations, as more time is spent at lower temperatures before the Soret diffusion is reduced.

3.10. Activation Enthalpy

As the activation enthalpy ΔH is lowered, the system undergoes a transition from nonvolatile to volatile behavior, where it remains at or close to thermal equilibrium throughout a sweep. To visualize this, a triangular voltage pulse from 0 to 2 V in 1 s and from 2 V back to 0 V also in 1 s was applied, followed by 8 s with no applied signal. The results are presented in **Figure 16**. Since higher activation enthalpies equate to lower vacancy mobility, there is an increase in the SET voltage. On the other hand, the devices with higher activation enthalpy have a higher electrical conductivity after SET, resulting in slightly increased temperatures. In a real device, a change in ΔH can be achieved either by modifications to the oxide like

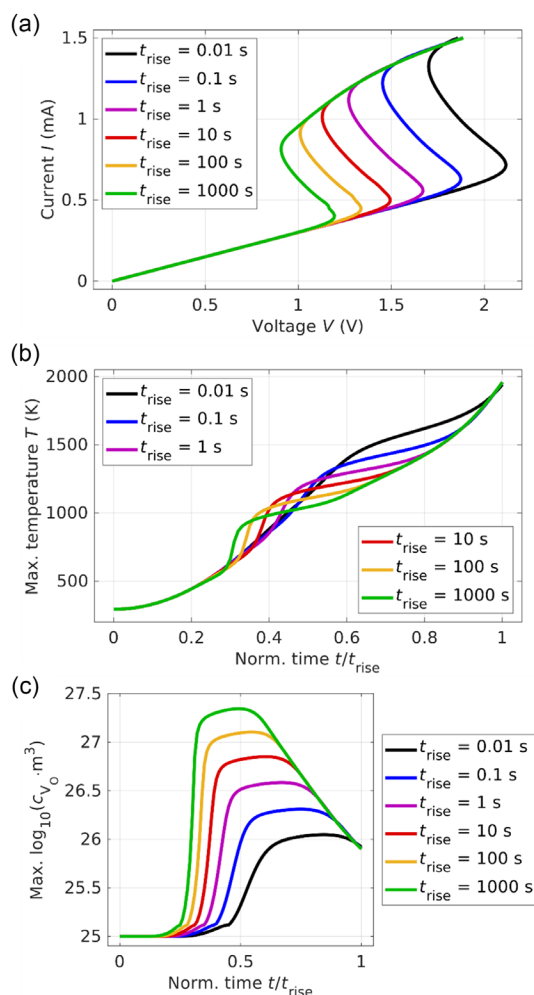


Figure 15. Effect of the ramping time t_{rise} for a linear current ramp up to 1.5 mA. a) I - V curves. b) Maximum temperature over time normalized by t_{rise} . c) Maximum concentration of oxygen vacancies over time normalized by t_{rise} .

varying its density or the introduction of dopants, or by replacing the oxide entirely.

For the first two seconds, the evolution of the maximum concentration of oxygen vacancies can be explained mostly by the proportionality of the Soret factor in terms of temperature and is similar for all cases shown here. However, the behavior after removal of the signal strongly depends on the activation enthalpy. While at $\Delta H = 0.65$ eV, there is only a slight reduction in concentration, at $\Delta H = 0.4$ eV, the initial concentration of $c_0 = 10^{25} \text{ m}^{-3}$ is reached almost immediately, indicating a volatile SET.

4. Modified Simulation Setup

4.1. Changes to the Configuration

In order to avoid elevated temperatures at the outer edge of the oxide, we performed further simulations using an extended

geometry, as shown schematically in **Figure 17**. The substrate material was also replaced to allow for equilibrated temperatures at the heat sink interface. This serves as a validity check for the results in Section 3. Obtaining qualitatively very similar results with the more rigorous boundary conditions of the extended geometry would give an indication that the structures described here and in Section 2 both lead to the same conclusions.

An updated list of the material parameters is shown in **Table 2**. Note that only the values for the substrate have changed, as the materials of the other layers remain unchanged.

In the diffusion coefficient, the limiting factor for high oxygen vacancy concentrations was removed, simplifying it to

$$D = D_0 \exp\left(-\frac{\Delta H}{k_B T}\right) \quad (7)$$

This was done to ensure the stability of simulations, as the concentration limit was reached even with the limiting factor, causing simulation failure. Instead, we checked afterward that the vacancy concentration did not exceed physically reasonable levels. Meanwhile, the oxide electrical conductivity is rewritten as

$$\sigma_{\text{TaO}_x} = \sigma_0 \min\left(\frac{c}{c_0}, 1000\right), \quad \sigma_0 = 75 \frac{\text{S}}{\text{m}} \quad (8)$$

with the initial oxygen vacancy concentration $c_0 = 10^{25} \text{ m}^{-3}$. To keep the device conductance from getting too high, which would again lead to problems with simulation stability, the conductivity is thus capped for $c > 1000 \cdot c_0$, but otherwise its definition is the same as in the previous sections.

4.2. Profiles of Temperature and Oxygen Vacancy Concentration

We applied a linear current ramp from 0 mA to 0.4 mA over a time of 1 s, at a lowered activation enthalpy of 0.9 eV, and observed the evolution of temperature and concentration profiles along a horizontal and a vertical cut line. The location of the cut lines within the oxide is sketched in **Figure 18a**. With the expanded geometry, there are two regions of negative differential resistance, as shown in **Figure 18b**. The points corresponding to the times at which the snapshots in **Figure 19** were taken are marked. According to this, the SET occurs within the first, smaller region of negative differential resistance.

As in Section 3.1, the gradients of temperature and oxygen vacancy concentration are higher in the radial than in the axial direction. However, while in the smaller device, the concentration is affected in the whole oxide, here, the redistribution is limited to radii smaller than two or three times the top electrode radius. Consequently, surrounding the center with elevated concentration, a ring is formed where oxygen vacancies are depleted. The area in the center, where the vacancy concentration and therefore also the electrical conductivity are higher than their initial values, increases in size with rising current. This could be an explanation for the much bigger second region of negative differential resistance, which only reverts to a positive differential resistance at unrealistically high currents.

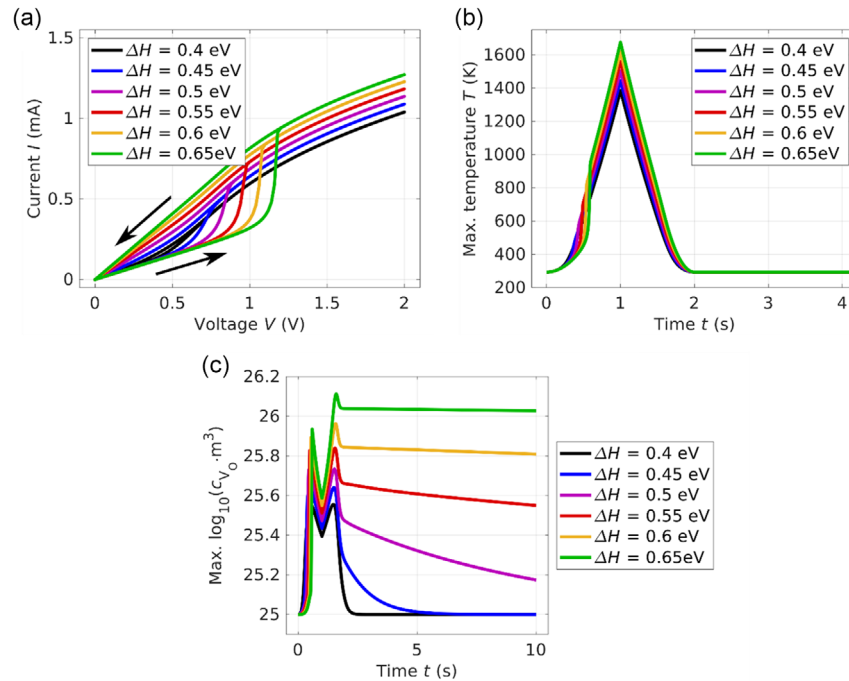


Figure 16. a) Voltage-controlled sweeps for different activation enthalpies. The signal is identical to the one used in Section 3.3, but here the sweeps are extended to $t = 10$ s by a period without applied signal. b) Maximum temperature over time. Only the first four seconds are shown because the temperature remains at ambient temperature for the remainder of the sweep in all cases. c) Maximum vacancy concentration during the triangular voltage pulse and for eight seconds after the pulse, showing the retention behavior at short timescales.

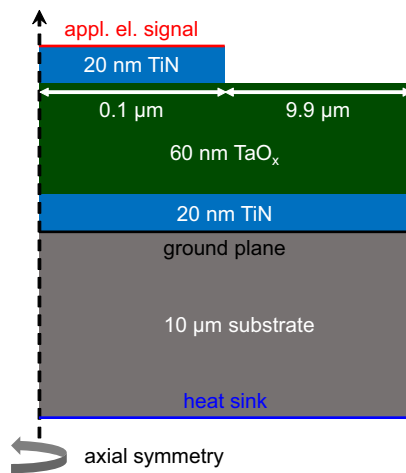


Figure 17. Schematic representation of the modified axisymmetric 2D structure, not to scale. Notably, the device radius and the height of the substrate are increased substantially. Also, the substrate material now has a higher thermal conductivity than SiO_2 .

4.3. Activation Enthalpy and Retention

For a further understanding of the influence of the activation enthalpy, we applied two triangular current pulses up to an absolute current of 0.4 mA as shown in Figure 20c. After that, no input is made for the rest of the sweep, which ends at $t = 300$ s. The resulting simulated I - V curves and maximum

Table 2. List of updated material parameters.

	TiN	TaO _x	Substrate
σ [$\frac{\text{S}}{\text{m}}$]	5×10^6	User defined	–
ϵ_r	4	22	–
κ [$\frac{\text{W}}{\text{m} \cdot \text{K}}$]	5	4	12
C_p [$\frac{\text{J}}{\text{kg} \cdot \text{K}}$]	545	174	532
ρ [$\frac{\text{kg}}{\text{m}^3}$]	5210	8200	4810

temperatures are presented in Figure 20a,b. Like in Section 3.10, an increase in activation enthalpy leads to higher SET voltages and currents. For the current-controlled sweep, this results in higher maximum voltages and thus a clear increase in the maximum temperature. Note that for the case of $\Delta H = 1$ eV, the temperatures briefly exceed 2100 K, at which point a real device could start to melt.^[11,12] Hence, the validity of the results for this case may be questionable. However, we decided to include it anyway for comparability with the results in Section 3. In all other simulations, the peak temperatures remain below 2100 K. During measurement, temperatures could be limited using a current compliance, as the maximum temperature immediately after the SET is less than 2000 K even for $\Delta H = 1$ eV.

Expanding on the study in Section 3.10 regarding retention, the maximum concentration of oxygen vacancies was observed during the gap between both current pulses and after the second pulse, as shown in Figure 21. Removal of the limiting factor for

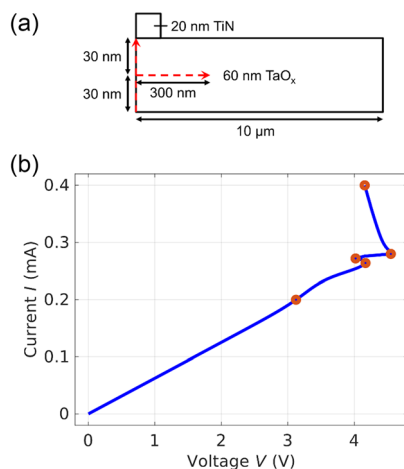


Figure 18. a) Sketch of the location of horizontal and vertical cut lines within the oxide as used in Figure 14, indicated by red dashed arrows. b) Simulated I - V curve for a linear current-controlled sweep with a ramping time of 1 s up to a maximum current of 0.4 mA. The red circles correspond to the times used in Figure 19.

vacancy transport at high concentrations means that a higher activation enthalpy is required for comparable retention performance. Importantly, the maximum concentration levels remain physically reasonable in all cases. Again, the maximum vacancy concentration stays elevated throughout the sweep, only falling to the initial value for low activation enthalpies. In the case of $\Delta H = 0.5$ eV, the retention is low enough for significantly increased hysteresis in the I - V curve during the second current pulse.

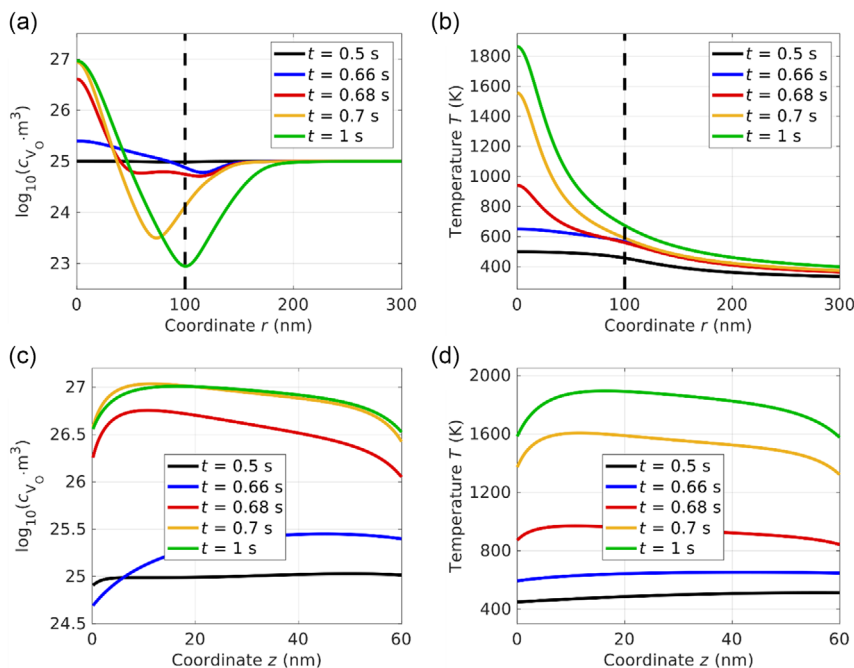


Figure 19. Profiles of oxygen vacancy concentration and temperature along the horizontal and vertical cut lines shown in Figure 18 at selected times t , showing the evolution over time. The vertical dashed lines in subfigures (a,b) mark the top electrode radius. a) Vacancy concentration along a horizontal cut line. b) Temperature along the same horizontal cut line. c) Vacancy concentration along a vertical cut line at $r = 0$. d) Temperature along the same vertical cut line.

In Figure 22, we verify that the extended geometry does in fact keep the temperatures near the bottom of the substrate and near the outer edge of the oxide close to ambient temperature. Therefore, even accounting for thermally equilibrated boundary conditions, the simulated devices cannot be RESET with an external signal when only thermodiffusion and Fick diffusion are included in the model. In this context, reaching a uniform oxygen vacancy distribution after the SET requires a device exhibiting volatile switching.

5. Conclusion

Using a time-dependent FEM model, we show that the inclusion of only thermal effects in the form of thermodiffusion countered by diffusion along concentration gradients does indeed produce unipolar behavior that does not depend on the polarity of the applied signal. We present a possible SET transition that can be tuned to be volatile or nonvolatile by varying the activation enthalpy for oxygen vacancy transport. However, with our model, we cannot get the system to undergo a RESET in the nonvolatile case, suggesting the requirement of other effects like interface reactions for a complete description of unipolar resistive switching in metal-oxide-metal memristive devices. We checked these findings using a modified setup with low-temperature gradients at the bottom of the substrate as well as the outer edge of the oxide and obtained qualitatively very similar results. In the default case, we use material parameters of a TiN/TaO_x/TiN stack, but with our comprehensive parameter study, the results remain valid for other oxide and electrode materials. All our

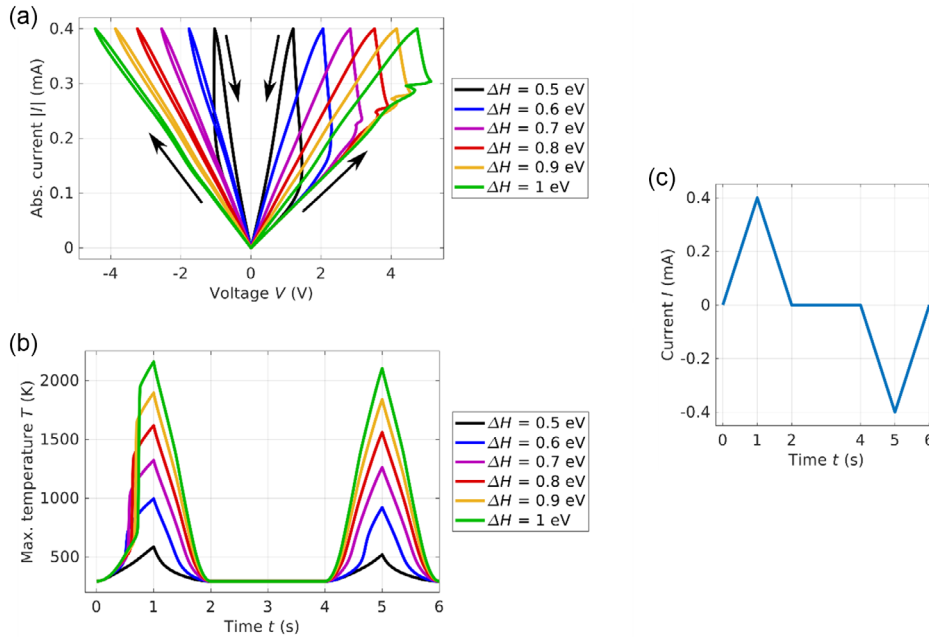


Figure 20. Application of a current sweep as visualized in subfigure (c) consisting of two triangular current pulses with opposing polarities. a) I - V curves for different activation enthalpies ΔH . Arrows indicate the path direction. b) Corresponding maximum temperatures. The peaks coincide with the current pulses. c) Applied current signal over time.

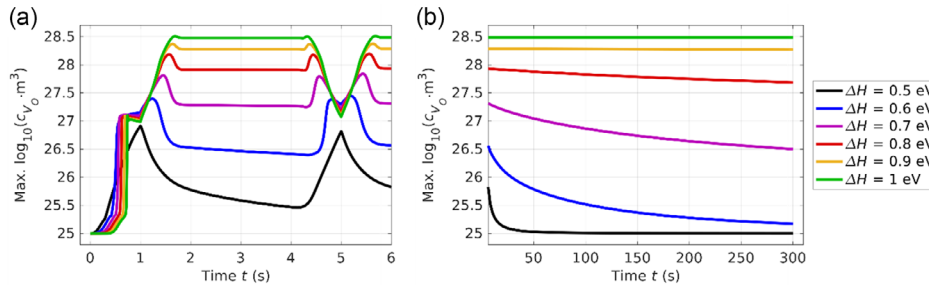


Figure 21. Extension of the current sweep described by Figure 20c up to 300 s by applying 0 mA for the remaining time. a) Dependence of the maximum oxygen vacancy concentration on the activation enthalpy. b) Extension of subfigure (a) to a time range between 6 and 300 s, visualizing the retention behavior.

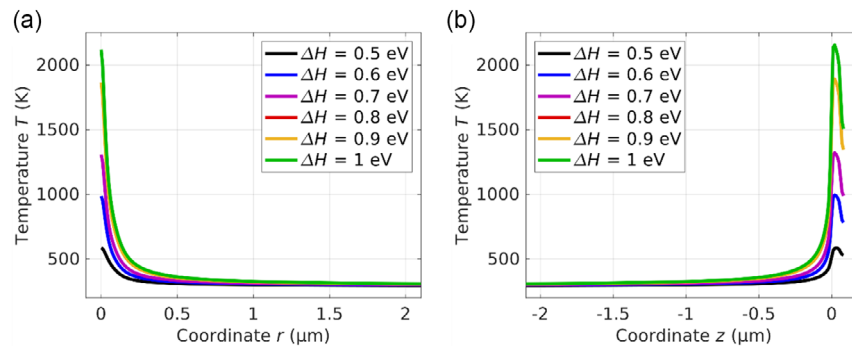


Figure 22. Verification that the temperatures near the bottom of the substrate as well as near the outer edge of the oxide remain reasonably close to the ambient temperature of 293.15 K. Snapshots taken at $t = 1$ s. a) Temperatures along a horizontal cut line as shown in Figure 18, but with the cut line extending outward to $r = 2 \mu\text{m}$. b) Temperatures along a vertical cut line at $r = 0 \mu\text{m}$, starting $2 \mu\text{m}$ below the interface between substrate and bottom electrode and ending at the upper edge of the top electrode. Here, $z = 0 \mu\text{m}$ corresponds to the interface between bottom electrode and oxide.

studies show a SET if the applied voltage or current is high enough, but no controlled RESET.

Received: May 31, 2023
Revised: August 28, 2023
Published online: September 14, 2023

Acknowledgements

This work was supported by funding from the DFG (German Science Foundation) within the collaborative research center SFB 917 —“Nanoswitches” (project B1—“Fast transient electrical analysis of resistive switching phenomena”), as well as funding from the Federal Ministry of Education and Research (BMBF, Germany) within the NEUROTEC project (grant nos. 16ME0398K and 16ME0399). Both are gratefully acknowledged. Open Access funding enabled and organized by Projekt DEAL.

Conflict of Interest

The authors declare no conflict of interest.

Data Availability Statement

The data that support the findings of this study are available from the corresponding author upon reasonable request.

Keywords

memristive device, thermodiffusion, unipolar switching, valence change mechanism

- [1] R. Dittmann, S. Menzel, R. Waser, *Adv. Phys.* **2022**, 70, 155.
- [2] H. Y. Lee, P. S. Chen, T. Y. Wu, Y. S. Chen, C. C. Wang, P. J. Tzeng, C. H. Lin, F. Chen, C. H. Lien, M.-J. Tsai, *Tech. Dig. - Int. Electron Devices Meet.* **2008**, 1, 1.
- [3] S. Gao, G. Liu, Q. Chen, W. Xue, H. Yang, J. Shang, B. Chen, F. Zeng, C. Song, F. Pan, R.-W. Li, *ACS Appl. Mater. Interfaces* **2018**, 10, 6453
- [4] R. Waser, R. Dittmann, G. Staikov, K. Szot, *Adv. Mater.* **2009**, 21, 2632.
- [5] D. B. Strukov, F. Alibart, R. S. Williams, *Appl. Phys. A* **2012**, 107, 509.
- [6] J. M. Goodwill, G. Ramer, D. Li, B. D. Hoskins, G. Pavlidis, J. J. McClelland, A. Centrone, J. A. Bain, M. Skowronski, *Nat. Commun.* **2019**, 10, 1628.
- [7] T. Diokh, E. Le-Roux, S. Jeannot, C. Cagli, V. Jousseau, J.-F. Nodin, M. Gros-Jean, C. Gaumer, M. Mellier, J. Cluzel, C. Carabasse, P. Candelier, B. De Salvo, *Thin Solid Films* **2013**, 533, 24.
- [8] F. Kurnia, Hadiyawarman, C. U. Jung, R. Jung, C. Liu, *Phys. Status Solidi RRL* **2011**, 5, 253.
- [9] W. Lengauer, S. Binder, K. Aigner, P. Ettmayer, A. Guillou, J. Debuigne, G. Groboth, *J. Alloys Compd.* **1995**, 217, 137.
- [10] R. A. Matula, *J. Phys. Chem. Ref. Data* **1979**, 8, 1147.
- [11] A. Reisman, F. Holtzberg, M. Berkenblit, M. Berry, *J. Am. Chem. Soc.* **1956**, 78, 4514.
- [12] Q. Xu, Y. Ma, M. Skowronski, *J. Appl. Phys.* **2020**, 127, 055107.